

Acoustic and Thermoacoustic Jet Propulsion

Jeroen Schoenmaker (✉ jeroen.schoenmaker@ufabc.edu.br)

Federal University of ABC <https://orcid.org/0000-0002-4525-208X>

Danilo Almeida Machado

National Institute for Space Research

Heriques Frandini

Fermilab

Annibal Hetem Junior

Federal University of ABC

Fábio Mota

Federal University of ABC

Research Article

Keywords: Synthetic jets, Jet propulsion, Thermoacoustic engines, Instrumentation

Posted Date: June 23rd, 2022

DOI: <https://doi.org/10.21203/rs.3.rs-1768888/v1>

License:   This work is licensed under a Creative Commons Attribution 4.0 International License.

[Read Full License](#)

Abstract

This manuscript bridges the fields of jet propulsion, synthetic jets and thermoacoustic engines. We put forward the case that acoustic air jets can be considered as a consistent approach for propulsion systems. Hitherto, studies on synthetic jet propulsion have been scattered and rather subsidiary. Furthermore, investigating with the perspective of propulsion can give new insights to the field of synthetic jets, and the physics of propulsion. We developed and characterized the propulsion properties with regard to several relevant parameters such as geometric factors, frequency and intensity of acoustic jets produced electromechanically and thermally. We demonstrated 10.4 mN and 2.7 mN thrust in the acoustic and thermoacoustic modes respectively, using compact tabletop assemblies. The physical mechanism of the jets has been modelled, simulated, verified with Schlieren imaging and laid in the perspective of adherent literature. Similarities and differences with regard to traditional jet propulsion systems are discussed. As an essentially unexplored avenue, several improvement directions are indicated.

1. Introduction

Great relevance has been given to the development of alternative engine solutions that are efficient, reliable and mechanically simple (Backhauss and Swift 1999). In the case of alternative non-conventional propulsion systems, a change of perspective can draw large attention (Xu et al. 2018).

In 1950, Ingård and Labate (1950) published a manuscript investigating acoustic streaming phenomena around orifices. Their setup was akin to the acoustic apparatus we have built for this work, although back then they did not aim for propulsion applications. Rather, their investigation focused on the nature of the jets formed in such conditions. While addressing the velocity of the stream, they measured a maximum thrust of 1,37 mN in their system, being the first systematic registry of synthetic air jet thrust known by the authors of this work. In his 2008 book “Notes on Acoustics”, Ingård returns on the subject and dedicates a subsection to acoustic propulsion. A nowadays well-known physics class demonstration is presented, where a rather small thrust is observed in Helmholtz resonators comprised of Christmas tree spherical ornaments. The phenomenon is described as an “amusing and perhaps puzzling” demonstration whose details and mathematical model are still a challenge (Ingard 2008).

Presently the field of synthetic jet research is established, advancing the overall comprehension of the phenomena involved (Glezer and Amitay 2002, Holman *et al.* 2005, Trávníček et al. 2012, Jankee and Ganapathisubramani 2019) and settling applications, mainly adherent to flow control (Pack and Seifert 2001, McCormick 2000), heat transfer (Jeng and Hsu 2016) and mixing (Wang and Menon 2001). Interestingly, bioinspired by sea creatures such as squids and salps, a propulsion system has been proposed for small water vehicles using jets produced by speaker coils as actuators (Thomas et al. 2005, Dabiri 2009, Qin et al. 2020).

It is important to remark that synthetic jet research relies largely on electromechanical transducers, as the jets are typically generated by speaker coils, piezoelectric actuators and pistons. This work aims to put forward the study acoustic jets produced not only mechanically, but thermally as well. In this sense it is appropriate to bring attention to another synthetic jet propulsion system not traditionally recognized as such. In 1891 Thomas Piot filed a patent for a steam generator that would be responsible for propelling a toy known as pop pop boat (Piot 1892). It is a candle fed steam engine with no movable parts that generates a steam cycle, causing pulsed water jets that propel a small boat (Dobson 2003). From the fundamental physics perspective, the thermoacoustic jet engines presented in this work can be regarded as the Stirling version of the pop pop boat engine. To our knowledge, only one study investigating synthetic jets driven by a thermoacoustic engine has been published (Chen et al. 2020). Although this represents a bold step towards the thermal realm, this study does not focus on propulsion and present results restricted to numerical simulations.

Thermoacoustic engines are known for being highly efficient and mechanically simple, possibly assembled with no moving parts (Swift 1988), thus strong candidates for reliable and sustainable applications. In the context of this manuscript, the only thermoacoustic air jet propulsion proposal we know of is the recent system crafted, concomitant to our project, by an independent developer based in a horizontal version of the Rijke tube (Blade 2021).

What if the high efficiency of Stirling engines can be harnessed in terms of jet propulsion by synthetic jets? To address this question, we divided the project into two separated inquiries, namely, one regarding the consistency of synthetic jets in terms of propulsion and the other whether it is possible to attain sustained and consistent propulsion from a thermoacoustic engine. It is worth noticing that, in the current propulsion systems paradigm, acoustic phenomena should be avoided as they are considered deleterious for optimal performance in most cases. In this work we turn the argument the other way around and assess how acoustic motion can be used in favor of propulsion.

2. Acoustic Jets

2.1 Acoustic propulsion measurements

In order to address the propulsion properties of synthetic jets, we investigated the resulting propulsion of jets produced through a 4" diameter loudspeaker (20 W max nominal power, 4 Ω impedance). The loudspeaker was driven by a sinusoidal voltage signal produced by a function generator with fine control on frequency and amplitude. Similarly to the work of Ingard and Labate (1950), the thrust of the jet was measured by the force exerted on a screen placed in the jet stream (Fig. 1).

In Fig. 2 we show the results of the thrust (T) as a function of the frequency of the driving voltage (F) for four different voltage amplitudes (V). The four curves present similar asymmetric and very regular thrust distribution with a maximum around $F = 70$ Hz. Throughout the remaining of this manuscript, we discuss

many relevant parameters that influence the thrust yield of this kind of system, but now we would like discuss with regard to basic aspects of jet propulsion.

Considering a conventional jet propulsion system operating in ideal condition, we can model the thrust (T), power (P) and air flow by the equations 1, 2 and 3 respectively:

$$T = \frac{dm}{dt} v$$

1

$$P = \frac{1}{2} \frac{dm}{dt} v^2$$

2

$$\frac{dm}{dt} = \rho A v$$

3

where m is the mass, v is the velocity of the flow at the nozzle, A is the transversal area of the nozzle and ρ is the density of the medium. Combining the equations one can get

$$P^2 = \frac{T^3}{4\rho A}$$

4

from where we apprehend the general correlation $P^2 \propto T^3$ of jet propulsion systems.

In our setup we use a loudspeaker to produce synthetic jets by means of electric power. Typically, loudspeakers yield about 1% of the electric power in sound pressure. It is reasonable to assume that the produced sound pressure is proportional to the electric power input to the loudspeaker and that the power of the system is given by $P = V^2/Z$, where Z is the effective impedance of the speaker coil.

Furthermore, by inferring that our set up can be modeled as an ideal jet propulsion system and as a regular electric system, we can expect a correlation between driving voltage and thrust as $V \propto T^{3/4}$. In the inset of Fig. 2 we observe that the maximum thrust value of each curve to the $3/4$ power as a function of the driving voltage results in a noteworthy linear behavior. The dashed line is a guide to the eye where the slope was adjusted to the experimental data. As discussed, the constant of proportionality depends on several parameters related to the intricate fluid dynamics of the experiment, as the physics of synthetic jets is distinct from traditional jet propulsion systems, and the intricacies determining the yield of the loudspeaker, that may also account for the systematic shift of the data towards lower values of thrust. For this reason, we have to be cautious when considering the inset as a result *per se*. Still, the

correlation is remarkable and an indication, along with the striking regular behavior of the four curves, that the measurements are sound.

2.2 Schlieren photography measurements

A systematic Schlieren photography study has been conducted using a Toepler system with two 300 mm diameter mirrors, both with 1500 mm of focal distance and optical surface quality of 40 – 20 scratch-dig. We used a 1.9 W, 425 nm LED illumination with vertical knife edge filter. Images were acquired with a Fastec TX3 fast camera. For the sake of contrast improvement, the air inside the nozzle was heated with a 10 W resistor for 1 minute prior to every measurement. The study sustains that the measured propulsion is the result of synthetic jets produced by the loudspeaker.

In Fig. 3 we observe typical results, evidencing the vortex ring structures in different experimental conditions that are consistent with all experimental data presented in this work. The thrust force measurement system was not available in the location of the Schlieren photography facility. However, by the acquired knowledge (and verifiable in section 2.4) we can claim that the experimental conditions of Fig. 3a were close to optimized thrust. By careful analysis of Schlieren images, we determined that the propagation velocity of the ring structure in this condition was 7.2 m/s.

2.3 Theoretical and numerical considerations

Since the initial publications by Rogers (1858) and Helmholtz (1858), several studies and models on vortex rings have been carried out, and their evolution in parallel with mathematical and computational tools over this period is remarkable. A classic view of the phenomenon is presented by Lamb (1993), who models the Stokes stream function of the vortex ring in cylindrical coordinates as being

$$\psi(r, x) = \frac{\kappa}{2\pi}(r + R)[K(E(\lambda)) - E(\lambda)]$$

5

where r and R are respectively the flow radius and the ring radius of the vortex ring, κ is the vortex filament of strength, or “circulation”, in its constant half-plane, λ is the ratio

$$\lambda = \frac{R - r}{R + r}$$

6

and $K(\lambda)$ and $E(\lambda)$ are the complete elliptic integral of the first kind over λ and the complete elliptic integral of the second kind, respectively. The vorticity is assumed to be a combination of the filament strength and the coordinates of the vortex filament, with expression

$$\omega(r, x) = \kappa \delta(r - r') \delta(x - x')$$

7

with (r', x') as the cylindrical coordinates of the vortex filament. $\delta(x)$ is the Dirac delta function. This model of an ideal vortex ring establishes the boundary situation in which the rotating flux ring has zero radius, and the ring is a circular line.

If we consider that the vortex ring has a thickness, the vortex ring can be approximated by a disk with a radius much smaller than the radius of the ring. So, we have $r/R \ll 1$, which leads us to $1 - \lambda^2 \approx 4r/R$, and in the limit $r_1 \rightarrow 0$, $\lambda \rightarrow 1$. Under these conditions, the elliptical integrals have as a solution

$$K(\lambda) = \frac{1}{2} \ln \left(\frac{16}{1 - \lambda^2} \right)$$

8
and

$$E(\lambda) = 1$$

9
We can also consider the approximation of a uniform vorticity, formally $\omega(r, x) = \omega_0$, which leads us to a Stokes stream function given by

$$\psi(r, x) = \frac{\kappa \omega_0}{2\pi} R \iint \ln \left(\frac{8R}{r_1} - 2 \right) dr' dx'$$

10
whose most important results for our study are the circulation

$$\Gamma = \pi \omega_0 a^2$$

11
with a being the radius of the disk, the hydrodynamic impulse

$$I = \rho \pi \Gamma R^2$$

12
and the kinetic energy

$$E = \frac{1}{2} \rho \Gamma^2 R \ln \left(\frac{8R}{a} - \frac{7}{4} \right).$$

13
This thin-core vortex ring model allows us to estimate the translational speed for the ring:

$$U = \frac{E}{2I} + \frac{3}{8\pi} \frac{\Gamma}{R}$$

14

For the simulations, we solve the Navier-Stokes equations properly simplified for the problem, considering the fluid (air) as compressible, adiabatic and with its non-zero viscosity. Integration over time was done using *FreeFem++* software (Hecht 2012), which was also used to generate the mesh, initial conditions and resulting data.

The simulations were carried out considering the symmetries of the problem and the recommendations proposed by Guyon and Mulleners (2021). The generated scene represents a 2D section that contains the main axis, corresponding to the advance movement of the ring. The initial conditions are: 1 atm and constant density throughout the environment, with zero speeds. The only region different from these conditions is the speaker output, represented by a wall that has its velocity in the x direction changed by a time interval equivalent to one pulse to mimic the ring generation. After that, the speed on the wall becomes zero again. In Fig. 4, the details of the edges of the calculation scenario are presented, together with the grid mesh.

We consider an incompressible, isothermal Newtonian flow (density $\rho = \text{const}$, viscosity $\mu = \text{const}$, no gravity), with a velocity field $\vec{V} = (u_r, u_\theta, u_z)$ in its cylindrical form:

$$\frac{1}{r} \frac{\partial (ru_r)}{\partial r} + \frac{1}{r} \frac{\partial (u_\theta)}{\partial \theta} + \frac{\partial u_z}{\partial z} = 0$$

15

$$\rho \left(\frac{\partial u_r}{\partial t} + u_r \frac{\partial u_r}{\partial r} + \frac{u_\theta}{r} \frac{\partial u_r}{\partial \theta} - \frac{u_\theta^2}{r} + u_z \frac{\partial u_r}{\partial z} \right) = - \frac{\partial P}{\partial r}$$

(16)

$$\rho \left(\frac{\partial u_\theta}{\partial t} + u_r \frac{\partial u_\theta}{\partial r} + \frac{u_\theta}{r} \frac{\partial u_\theta}{\partial \theta} - \frac{u_r u_\theta}{r} + u_z \frac{\partial u_\theta}{\partial z} \right) = - \frac{1}{r} \frac{\partial P}{\partial \theta}$$

(17)

$$\rho \left(\frac{\partial u_z}{\partial t} + u_r \frac{\partial u_z}{\partial r} + \frac{u_\theta}{r} \frac{\partial u_z}{\partial \theta} + u_z \frac{\partial u_z}{\partial z} \right) = - \frac{\partial P}{\partial z}$$

18
and

$$p = \rho R \theta$$

19

where R is the ideal gas constant and θ is the temperature.

Here, we present the most relevant results of the simulations. Figure 5 show the evolution of gas pressure and velocity at the same instants, namely $t = 4, 6$ and 8 ms. The instant $t_0 = 0$ is the moment when the pressure pulse at the loudspeaker output returns to zero. According to the simulations the ring is formed immediately after t_0 , presenting the nominal conditions expected from this phenomenon.

As the simulation progresses in time, two regions of low pressure, one ahead and the other behind, accompany the ring. This is a natural consequence of the phenomenon's propagation, but it can be intuitively explained as the edges of the high-speed region of the interior of the ring.

By introducing a normalized kinetic energy quantity, given by

$$E' = \frac{1}{2} \Gamma^2 R \ln \left(\frac{8R}{a} - \frac{7}{4} \right)$$

20

one can estimate the point of best (or maximum) transport of energy. Figure 6 presents the evolution of ring radius, hydrodynamic impulse and normalized kinetic energy in the vortex ring. It is possible to distinguish an instant at $t = 0.94$, which corresponds to the maximum kinetic energy. For subsequent times, the kinetic energy will quickly disappear, and the vortex ring is disaggregated.

In the experiments the vortex rings are formed sequentially by the sinusoidal voltage input and each following ring is slightly affected by the distribution of velocity and pressure left by the previous one. The low-pressure region ahead of the new ring binds to its counterpart in the preceding ring. As a final result, a "tube" is formed that conducts the air flow and preserves the life of the rings for a longer time.

On the other hand, for higher frequencies, a proper residence time for the air is not satisfied and the close presence of a former ring can be disruptive to the stability of the next coming ring, as we show in the experimental results in the next sessions. However, in suitable conditions, we can use this "vortex ring driven tube" model to estimate the final numbers, which connect the simulations with the experiments.

Assuming the pulse diameter (region 1 of Fig. 4) as 23 mm and using the frequency of 100 Hz as a time base, we can denormalize the simulation results. As a result, a maximum pressure of 10 Pa has been obtained in the circulating inner region of the ring (Fig. 5a). Moreover, as can be seen in Fig. 5b, a vortex ring structure with a central axial velocity of 13 m/s embedded in stagnant surroundings is compatible

with a 7.2 m/s propagation velocity of the vortex ring measured by Schlieren instrumentation. Under the hypothesis that the tube maintains its internal diameter constant throughout the experiment, this brings us to a force of 10 mN applied to the bulkhead/sensor.

From the observations, it is possible to conclude that vortex rings do not propagate indefinitely. In fact, there are three main reasons that end up with a vortex ring: dissipation, self-induced instabilities, and space intervals between rings. The dissipation occurs due to exchanges of energy in infinitesimal packets between the ring and the environment. This energy loss occurs at the ring surface and is mainly linked to the viscosity of the medium. Its effect is to reduce circulation which, along the process, ends up accelerating the generation of self-induced instabilities and the destruction of the ring. Self-induced instabilities were thoroughly investigated by Windall and Sullivan (1973), both formally and experimentally. These perturbations are characterized by resonant longitudinal oscillations that tend to increase in amplitude with the passage of time. The main result of these researchers is that the order of instability follows $\ln(a/R)$ and tends to dissipate the ring as a/R approaches unity.

If the space between two rings is small enough for there to be significant interference between the circulation of both, we will observe the self-destruction of the two rings. This is easy to understand, since, as the circulation is the same for all rings ("forward" on the inside and backwards on the outside), the surface velocities of the fluid will have opposite directions at the point where the rings touch. This last form of dissipation gives us the ideal frequency for the experiments. If the frequency is too high, the rings get closer and destroy each other. If it is too low, the contribution to the formation of the "tube" with the airflow will be less effective.

2.4 Relevant parameters for acoustic jet propulsion

In previous sessions we presented the behavior of the thrust generated by acoustic jets as a function of the amplitude and the frequency of the applied voltage. We also established, by Schlieren photography and simulations, the nature of the jets as being constituted of a sequence of vortex rings, thus being consistent with the synthetic jet literature. In this session, we present experimental results for the behavior of the system's propulsion as a function of two other relevant parameters highlighted in Fig. 1, the nozzle exit diameter (D) and tapering angle (α).

In Fig. 7 we present the measurements of the thrust as a function of the frequency of the driving voltage (using $V = 1.86$ V) for 9 different nozzle exit diameters. In all curves, the tapering angle was the same ($\alpha = 60^\circ$). For the sake of visualization, the experimental points are shown for three representative curves, namely for $D = 15.5$ mm (smallest nozzle exit diameter of the set), $D = 24.5$ mm (maximum yield) and $D = 35$ mm (largest diameter). All other curves are represented by lines, as the behavior of the thrust varies monotonically and consistently from one curve to another. All curves present the same general trend observed in Fig. 2, i.e., an asymmetric curve with a peak of maximum thrust around $f = 100$ Hz. It is worth mentioning that in the thrust measurements in between 160 and 200 Hz, a moderate instability was observed, in the sense that the position of the screen used to measure the force swayed slightly, turning the measurement in that region rather less precise, as can be sensed by the oscillation of the data points

in this range of the graph. This effect was more or less observed in all measurements and, as mentioned in the last session, simulations indicate that this is related to unsuitable residence time and coupling with the thrust measurement screen. Interestingly the instability of the screen diminished for frequencies higher than 200 Hz. However, one has to take into account that the thrust is also strongly mitigated in that range of frequencies.

In the inset, we depict the maximum thrust of each curve as a function of the corresponding nozzle exit diameter, showing the consistent variation of the behavior of the curves and that the maximum thrust happened for $D = 24.5$ mm (red closed circle).

The influence of the nozzle tapering angle (α) on the thrust can be examined in Fig. 8. In (a) we observe the behavior of the thrust as a function of the driving frequency for a fixed nozzle exit diameter $D = 27.5$ mm but for 4 different values of the tapering angle, namely $\alpha = 60^\circ, 85^\circ, 97^\circ$ and 180° . The last value means that, instead of a cone shaped nozzle, the loudspeaker has been covered with a flat screen with a round orifice in the center. Interestingly, the tapering angle seem not to have significant impact on the thrust yield of the propulsion system as all curves essentially overlap. An important remark is that the thrust measurement instability for $F > 160$ Hz turned out to be severe for $\alpha = 180^\circ$ (the flat screen), precluding measurements beyond 150 Hz value. In Fig. 8b, we performed the same study depicted in the inset of Fig. 7, i.e., the maximum thrust as a function of the nozzle exit diameter, but for 3 different tapering angles, namely $\alpha = 60^\circ, 85^\circ$ and 180° . Surprisingly, the largest value of trust has been obtained for the flat screen, and for considerably larger values of exit diameters. Arguably, nozzle engineering for propulsion systems seldom relies on flat obstructions to the flow, and this reveals how this study points to interesting new physics of jet propulsion.

3. Thermoacoustic Jets

In previous sessions we addressed the fundamental aspects of synthetic jet propulsion, and the employment of a loudspeaker has been justified and a functional device to produce suitable jets for the study. In this session we advance to the last objective of this work, which is to demonstrate thermoacoustic jet propulsion. We focused on 3 thermoacoustic mechanisms based on tubular structures depicted in Fig. 9. The first configuration is a tube open on both sides and it is widely known as a Rijke tube (Fig. 9a). It is often said that the Rijke tube operates only in vertical position when standing still, by taking advantage of convection. However, when the hot and cold contrast within the tube is well crafted, it also generates air flow in horizontal position as tested in our laboratory. The second configuration is known as Sondhauss tube and, differently from a Rijke tube, it is closed in one end (Fig. 9b). Consequently, the acoustic behavior is changed and the hot and cold contrast has to be adjusted accordingly. The third tested configuration consists of a tube rigidly closed in one side and operating with a vibrating diaphragm on the other side (Fig. 9c). In this case, the acoustic resonance also depends on the elastic behavior of the diaphragm requiring further adjustments on resonance parameters. In this configuration we expected to observe similarities with our acoustic results as the diaphragm can be considered an analogous of the loudspeaker's driving cone. In addition, a tapering nozzle has been

attached, mimicking the acoustic mechanism described in previous sessions. In the three configurations shown, the resulting jet is moving from left to right with respect to the drawing. We tested on glass tubes of several sizes in all three configurations.

In all tests we performed, the configurations (a) and (c) resulted in perceptible, however small thrust forces (0,5 mN) that did not enable systematic characterization. On the other hand, we obtained remarkable thrust values with the Sondhauss configuration (b), using a 95 cm length and 4.5 cm diameter tube. It is worth mentioning that the Sondhauss configuration can be considered the Stirling counterpart of the steam cycle associated with the pop pop boat. We used a 600 W FeCrAl electric stove spring resistance as a heat source positioned 23 cm from the closed end. The cold section, positioned around 28 cm from the closed end was maintained by a wet cloth on the outside, associated with a steel mesh inside the tube for improved heat exchange. The experimental results can be observed in Fig. 10 depicting the thrust as a function of the heat power delivered to the joule resistance. The resonance regime has only been obtained for powers above 200 W where the thermoacoustic frequency was constant at 92 Hz. This corresponds to a sound wavelength of $\lambda = 373$ cm, that can be associated with the acoustic resonance of 93,3 cm long tube closed in one end, in agreement with nominal 95 cm glass tube. For powers levels above 200 W, we observe a monotonic increase in thermoacoustic thrust, reaching a highest value of 2,7 mN at the maximum power of the joule heater, 600 W.

4. Conclusions

We demonstrated, characterized, modeled and simulated the propulsion generated by synthetic jets produced acoustically. Moreover, we demonstrated thermoacoustic jet propulsion. The results show consistent behavior of the thrust with respect to several relevant parameters, such as power, frequency, and geometric factors. This work opens new avenues for the field of jet propulsion physics, bridging it with the fields of thermoacoustic engines and synthetic jets. Moreover, this study indicates important differences to traditional jet propulsion systems, such as nozzle engineering.

Nomenclature

A	area of the jet flow	V	amplitude of applied voltage
a	radius of vortex disc	v	velocity of the jet stream
D	nozzle exit diameter	x	direction of flow
E'	normalized kinetic energy	Γ	circulation – defined by eq.11
F	frequency of applied voltage	α	nozzle tapering angle
I	hydrodynamic impulse	δ	Dirac delta function
m	mass	θ	temperature
P	power	κ	vortex filament of strength
p	pressure	λ	radius ratio defined by eq. 6
R	vortex ring radius	μ	fluid viscosity
\bar{R}	ideal gas constant	ρ	fluid density
r	ring flow radius	ω	angular frequency of the driving voltage
T	thrust		
U	translational speed of vortex ring		

Declarations

Authors' contributions

JS conceived the project, worked on the instrumentation, performed most of the experimental measurements and wrote the manuscript. DAM performed the Schlieren photography experiments. HF designed and constructed most of the instrumentation used in the project. AHJ is responsible for the model and simulations presented in this work. FM guided the project in the framework of propulsion giving theoretical assistance and literature input. All authors maintained close contact and communication during the project. All authors declare no conflicts of interest.

Acknowledgements

This work was partially supported by the Brazilian agency Capes. The project was inspired by problem 2 of the 2021 list from the International Physicists' Tournament (IPT). The IPT started in 2009 in Ukraine as competition between physics students from a home university and Russian Federation. We thank IPT organizers for providing insightful physics discussion and international peaceful collaboration.

References

1. Backhaus, S. and G. Swift (1999). A thermoacoustic Stirling heat engine. *Nature* 399, 335–338. <https://doi.org/10.1038/20624>
2. Blade, A. (2021). *Thermoacoustic heat engine with thrust? - short heat engine experiment with standing wave*, march 6th. <https://youtu.be/uZwQwztWC2A> accessed in 24/08/21

3. Chen, G., G. Krishan, Y. Yang, L. Tang and B. Mace (2020). Numerical investigation of synthetic jets driven by thermoacoustic standing waves. *Int J of Heat and Mass Transf* 146:118859
<https://doi.org/10.1016/j.ijheatmasstransfer.2019.118859>
4. Dabiri, J. O. (2009). Optimal Vortex Formation as a Unifying Principle in Biological Propulsion. *Annu Rev Fluid Mech*, 41: 17–33 <https://doi.org/10.1146/annurev.fluid.010908.165232>
5. Dobson, R. T. (2003). An open oscillatory heat pipe steam-powered boat. *International Journal of Mechanical Engineering Education* 31:4 339–358 doi:10.7227/IJMEE.31.4.5
6. Glezer, A. and M. Amitay, (2002). Synthetic Jets. *Annu Rev Fluid Mech* 34, 503
<https://doi.org/10.1146/annurev.fluid.34.090501.094913>
7. Guyon, G. de, and K. Mulleners (2021). Estimating the non-dimensional energy of vortex rings by modelling their roll-up. arXiv:2112.03387v1 [physics.flu-dyn]
8. Hecht, F. (2012). New development in FreeFem++ (PDF). *Journal of Numerical Mathematics* 20 (3–4): 251–266. doi:10.1515/jnum-2012-0013. S2CID 12770876
9. Helmholtz, H. von (1858). Über Integrale der hydrodynamischen Gleichungen, welche den Wirbelbewegungen entsprechen (PDF). *Journal für die reine und angewandte Mathematik*. 55: 25–55. <https://doi.org/10.1515/9783112336489-003> ISBN 9783112336472
10. Holman. R., Y. Utturkar, R. Mittal, B. L. Smith and L. Cattafesta (2005). Formation Criterion for Synthetic Jets. *AIAA Journal* 43, 10 <https://doi.org/10.2514/1.12033>
11. Ingård, U. and S. Labate (1950). Acoustic Circulation Effects and the Nonlinear Impedance of Orifices. *The Journal of the Acoustical Society of America* 22, 211
<https://doi.org/10.1121/1.1906591>
12. Ingård, U., (2008). *Notes on Acoustics*. Infinity Science Press LLC, Hingham
13. Jankee, G. K. and B. Ganapathisubramani, (2019). Influence of internal orifice geometry on synthetic jet performance. *Exp Fluids* 60, 51. <https://doi.org/10.1007/s00348-019-2697-2>
14. Jeng, T-M., W-T. Hsu, (2016). Experimental study of mixed convection heat transfer on the heated plate with the circular-nozzle synthetic jet. *International Journal of Heat and Mass Transfer* 97 DOI: 10.1016/j.ijheatmasstransfer.2016.02.029
15. Lamb, H. (1993). *Hydrodynamics*. Cambridge University Press, New York, ISBN 10: 0521055156 ISBN 13: 9780521055154.
16. McCormick, D. C., (2000). Boundary layer separation with directed synthetic jets. *AIAA 38th Aerosp Sci Meet 2000 – 0519*, Reno, Nev USA
17. Pack, L. G. and A. Seifert, (2001). Periodic Excitation for Jet Vectoring and Enhanced Spreading. *Journal of Aircraft* 38, 3 <https://doi.org/10.2514/2.2788>
18. Piot, T. (1892). UK Patent 20,081 Issue date: Oct. 15
19. Qin. L., Y. Xiang, S. Qin and H. Liu (2020). On the structures of compressible vortex rings generated by the compressible starting jet from converging and diverging nozzles. *Aerospace Science and Technology* 106:106188 <https://doi.org/10.1016/j.ast.2020.106188>

20. Rogers, W. B. (1858). On the formation of rotating rings by air and liquids under certain conditions of discharge. *Am. J. Sci. Arts.* 26: 246–258.
21. Swift, G. W., (1988). Thermoacoustic engines. *The Journal of the Acoustical Society of America* 84: 1145 <https://doi.org/10.1121/1.396617>
22. Thomas, A. P., M. Milano, M. G. G'Sell, K. Fischer and J. Burdick (2005). Synthetic Jet Propulsion for Small Underwater Vehicles. *Proceedings of the 2005 IEEE International Conference on Robotics and Automation*, pp. 181–187, doi: 10.1109/ROBOT.2005.1570116
23. Trávníček, Z., Z. Broučková, and J. Kordík (2012). Formation Criterion for Axisymmetric Synthetic Jets at High Stokes Numbers. *AIAA Journal* 50, 9 <https://doi.org/10.2514/1.J051649>
24. Wang, H., and S. Menon, (2001). Fuel–Air Mixing Enhancement by Synthetic Microjets. *AIAA Journal* 39, 12 <https://doi.org/10.2514/2.1236>
25. Windall, S. E. and J. P. Sullivan (1973). On the Stability of Vortex Rings. *Proc. R. Soc. Lond. A* 332: 335–353 <http://www.jstor.org/stable/75015>
26. Xu, H., Y. He, K. L. Strobel, *et al.* (2018). Flight of an aeroplane with solid-state propulsion. *Nature* 563, <https://doi.org/10.1038/s41586-018-0707-9>

Figures

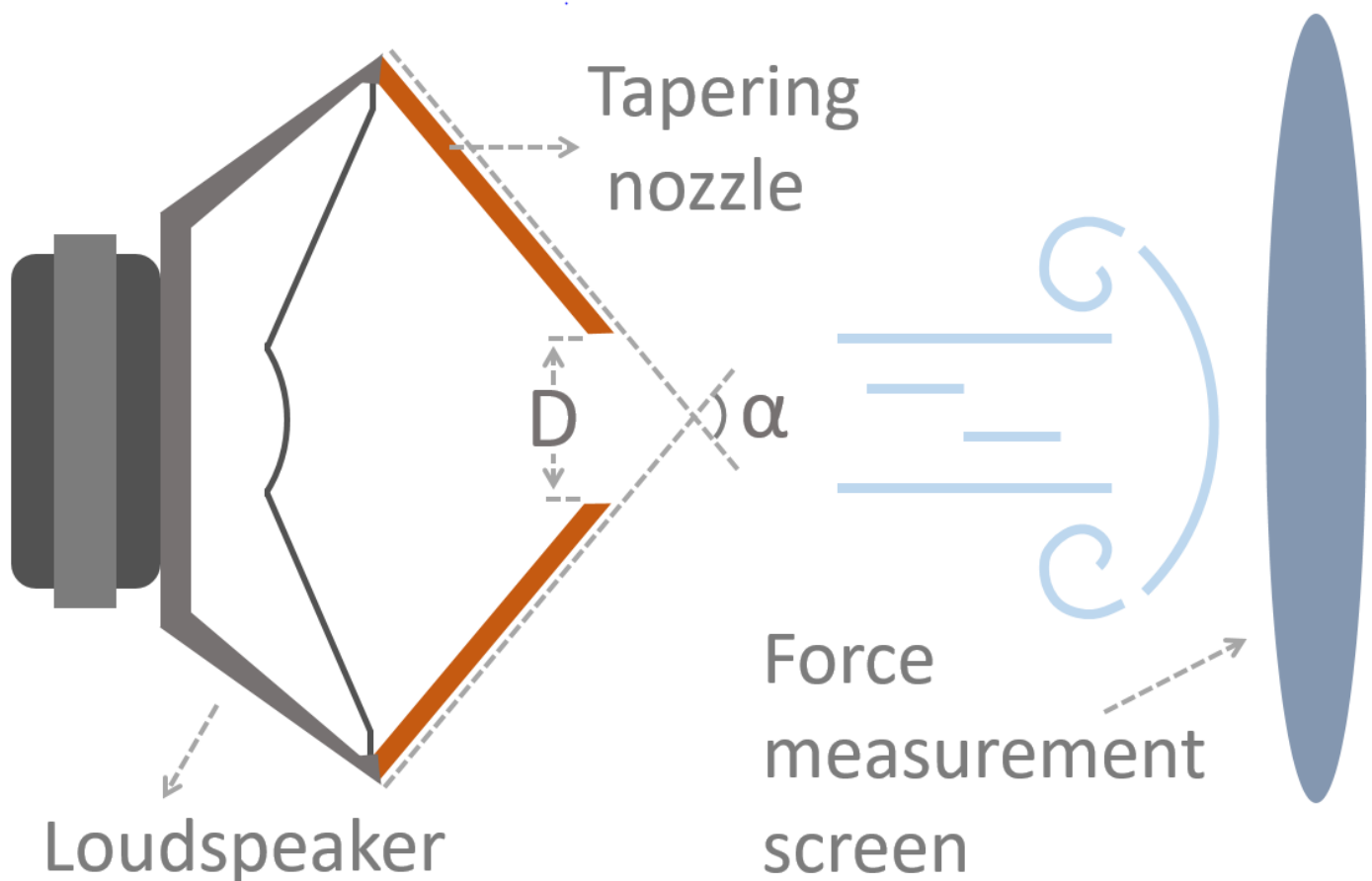


Figure 1

Experimental setup for the production of acoustic jets comprised of tapering nozzle directly attached to a loudspeaker. The sketch exhibits the parameters nozzle exit diameter (D) and tapering angle (α).

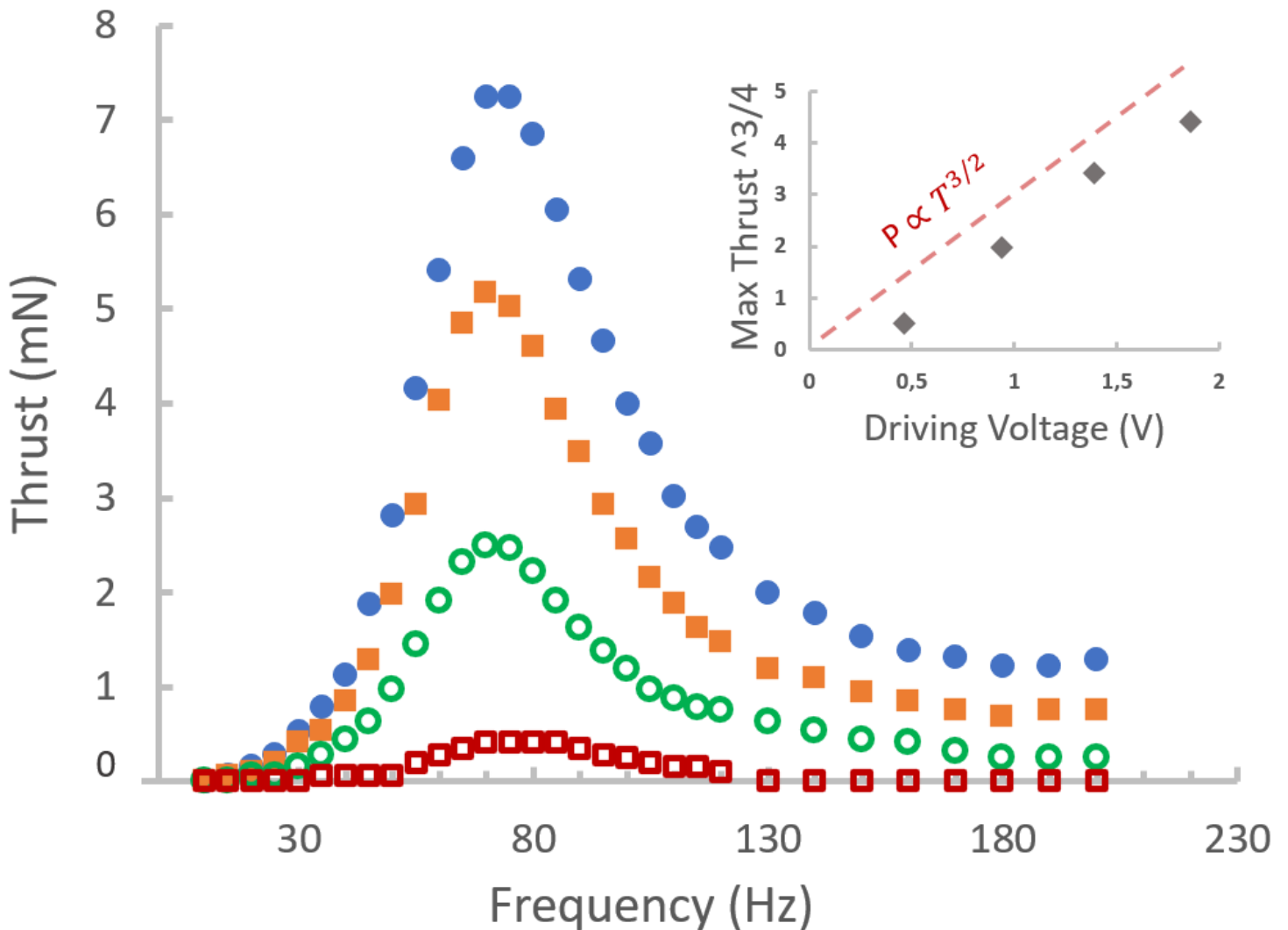


Figure 2

Thrust (T) as a function of the loudspeaker driving voltage frequency for 4 different driving voltage amplitudes of the loudspeaker: 0,46 V (red open squares), 0,94 V (green open circles), 1,39 V (orange filled squares) 1,86 V (blue filled circles). Jet propulsion is produced consistently in a wide range of power levels and frequencies. Nozzle exit diameter $D = 21$ mm. Inset: Maximum thrust of each curve to the power of $3/4$, as a function of the driving voltage.

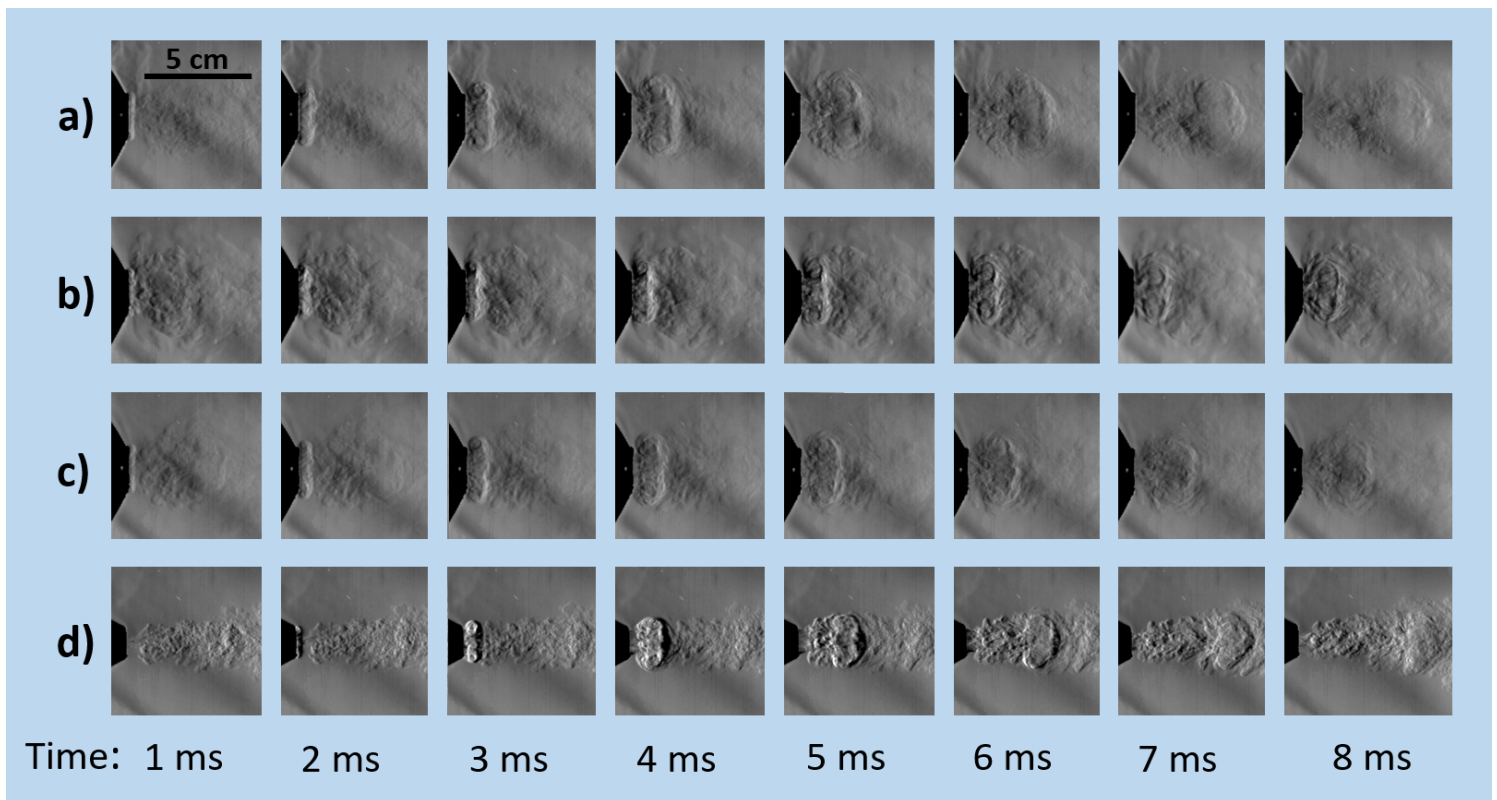


Figure 3

Schlieren imaging of the jets produced acoustically in conditions with varying intensities, frequencies, tapering angle and nozzle exit diameter size: a) Driving voltage $V = 1,86$ V, frequency $F = 100$ Hz, tapering angle $\alpha = 120^\circ$, nozzle exit diameter $D = 23,0$ mm. b) $V = 1,86$ V, $F = 50$ Hz and $\alpha = 120^\circ$, $D = 23,0$ mm, c) $V = 0,94$ V, $F = 100$ Hz and $\alpha = 120^\circ$, $D = 23,0$ mm, d) $V = 1,86$ V, $F = 100$ Hz and $\alpha = 60^\circ$, $D = 13,5$ mm. Time interval between images is 1 ms as marked in the bottom row. All conditions with resulting propulsion present Schlieren contrast that shows sequences of vortex rings with frequencies matching the driving voltage oscillation. In the supplementary materials, we provide an animated gif for each case where the dynamics of the vortex formation and propagation can be appreciated. This result is consistent with synthetic jet literature (Ingard 2008).

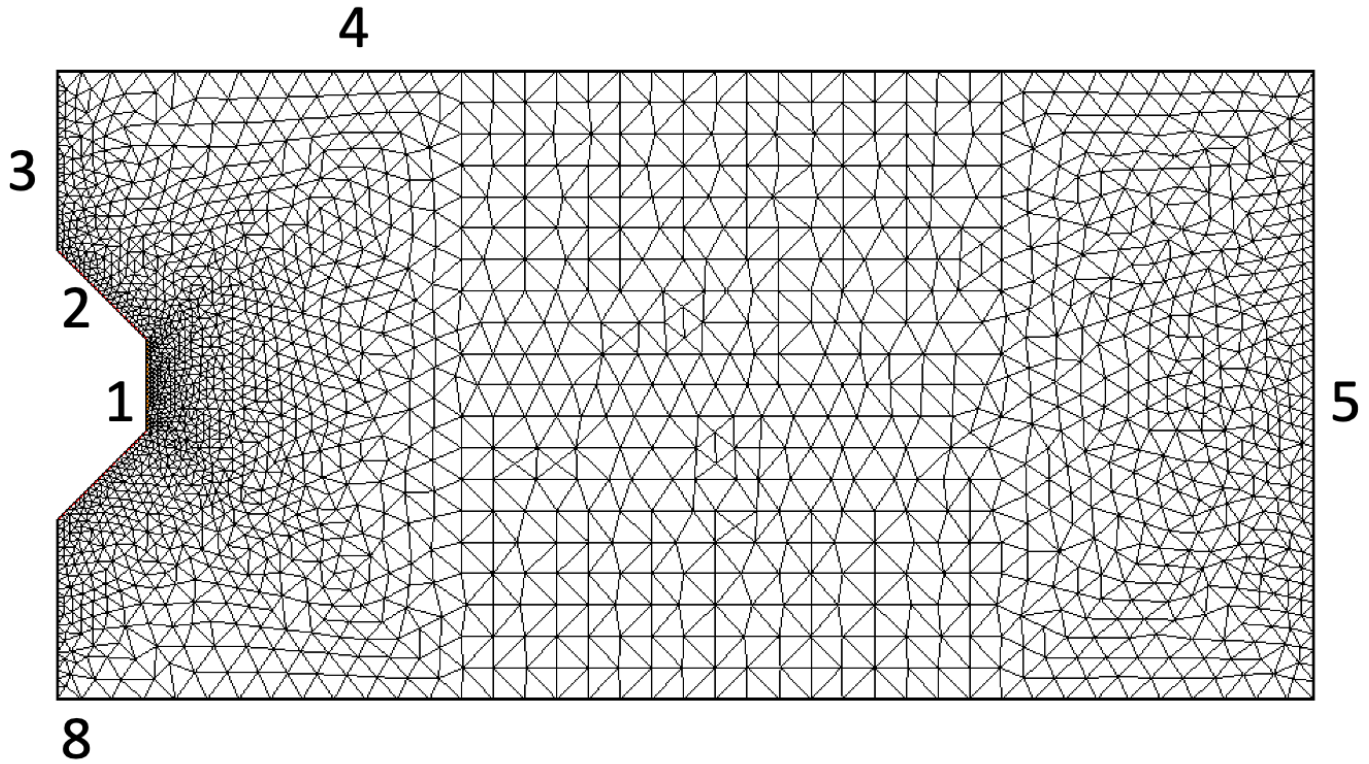


Figure 4

The grid mesh of the simulations. Wall 1 is the source of the pulse that has the velocity in the forward direction during a time interval. Walls 2 and 8 are solid walls and all other boundaries present free conditions.

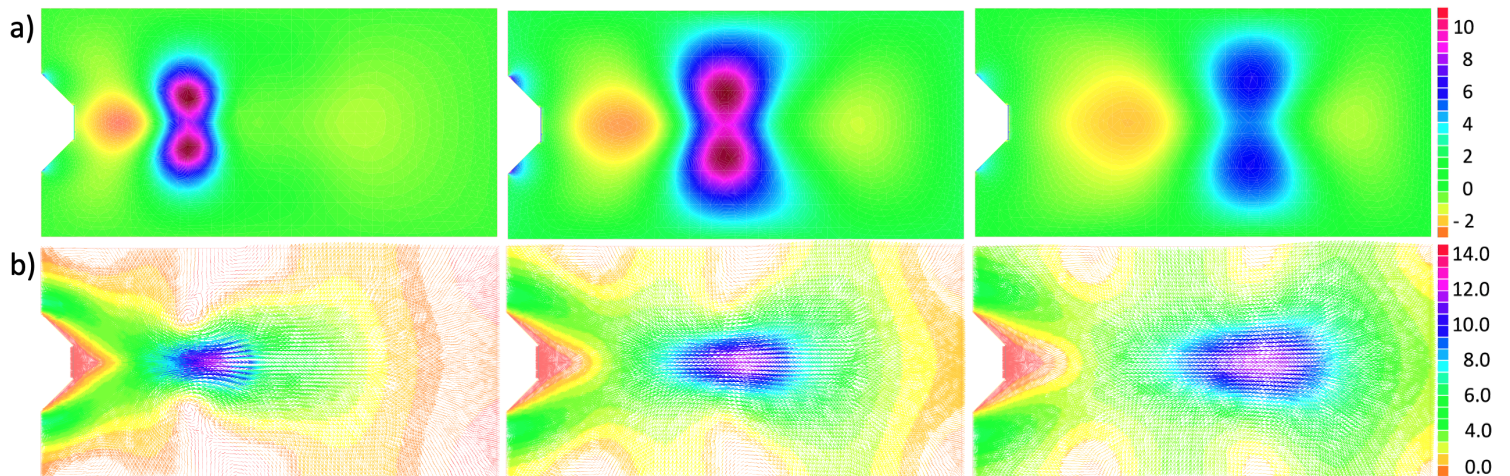


Figure 5

Three moments of the simulation, respectively $t= 4, 6$ and 8 ms from the beginning of the pulse, of the pressure and displacement of the ring. Line (a): the color represents the variation in pressure (in Pa) compared to normal pressure (1 atm) as indicated by the scale on the right of the last image. It is

observed that the radius of the ring increases and the internal pressure decreases with advancing time. Line (b): three moments of the simulation of the velocity in its vectorial form for the same instants of (a). The colored arrows and its length represent the variation in velocity (in m/s) in two dimensions compared to null movement.

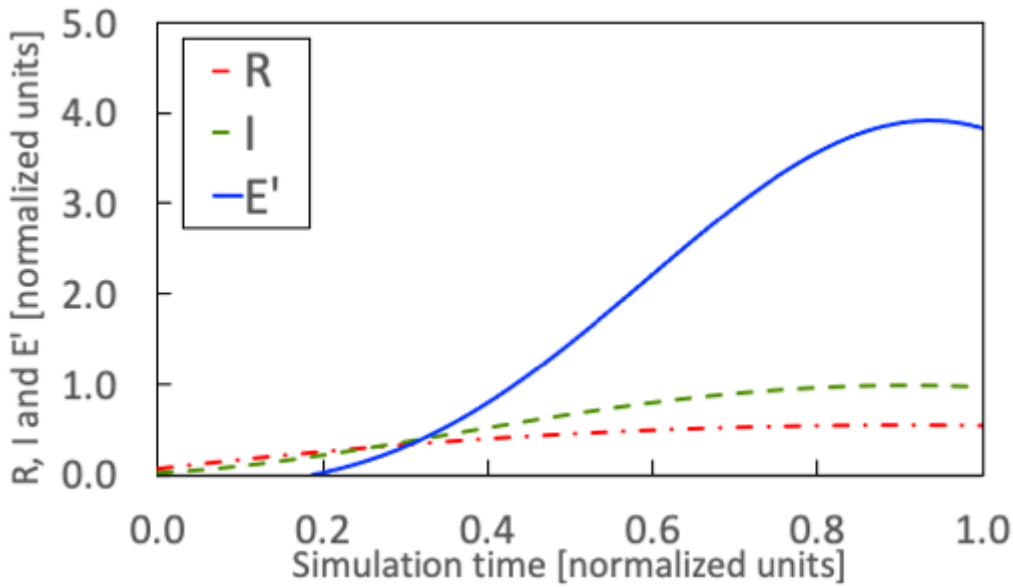


Figure 6

Evolution of ring radius, hydrodynamic impulse and normalized kinetic energy.

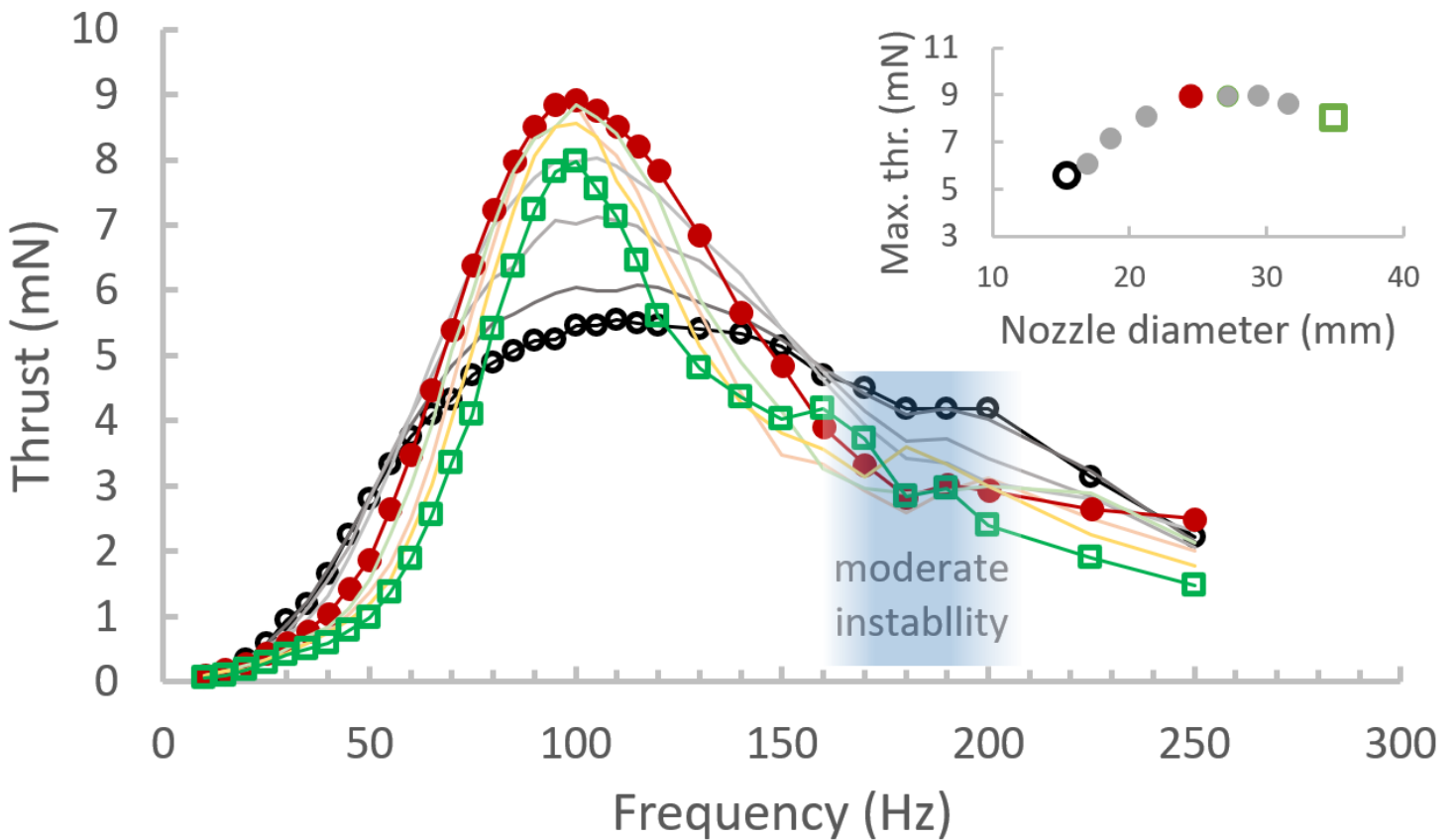


Figure 7

Behavior of the thrust as a function of the frequency F (for a $\alpha = 60^\circ$ and $V = 1.86 \text{ V}$) for 9 different nozzle exit diameters D , namely 15.5, 17, 18.7, 29.5, 21.3, 24.5, 27.3, 29.5, 31.7 and 35 mm. the experimental data points of three significant curves are highlighted with symbols: $D = 15.5 \text{ mm}$ (black open circles), $D = 24.5 \text{ mm}$ (solid red circles) and $D = 35 \text{ mm}$ (open green squares). The behavior of the other curves varies monotonically inbetween the highlighted curves and data points were suppressed from the graph for the sake of readability. (Inset) Excerpt from previous graph just showing the behavior of the maximum thrust of each curve as a function of the Nozzle exit diameter D .

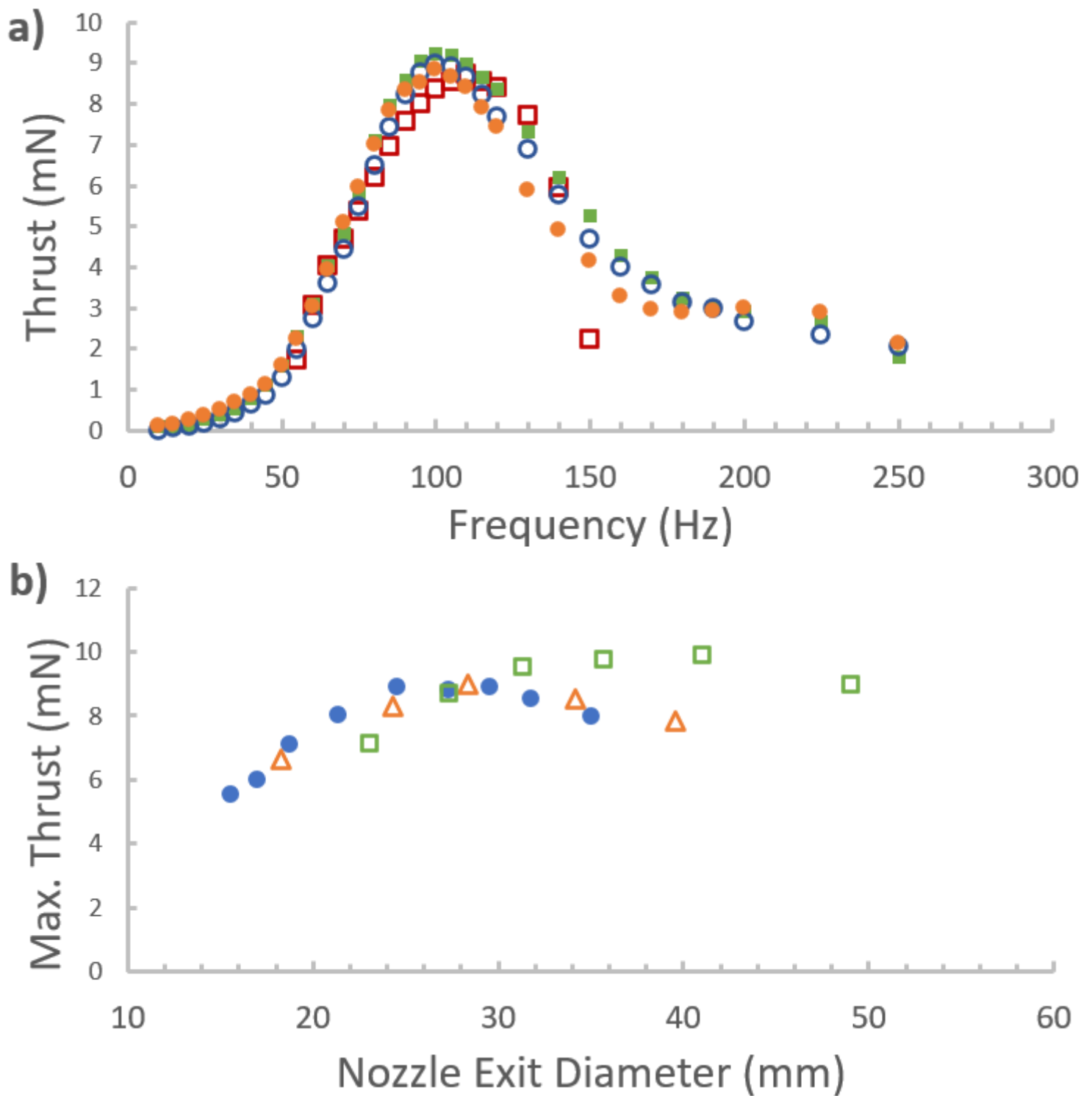


Figure 8

a) The behavior of the thrust as a function of frequency for 4 different tapering angles: $\alpha = 60^\circ$ (closed orange circles), $\alpha = 85^\circ$ (open blue circles), $\alpha = 97^\circ$ (closed green squares), $\alpha = 180^\circ$ (open red squares). All measurements performed with the same exit diameter $D = 27.5$ mm. The driving voltage amplitude has been kept constant at $V = 1.86$ V. This result shows that tapering angle plays little role, as all curves

essentially overlap. b) The same as the inset of Fig. 7 but for three different tapering angles: $\alpha = 60^\circ$ (closed blue circles), $\alpha = 85^\circ$ (open orange triangles) and $\alpha = 180^\circ$ (open green squares).

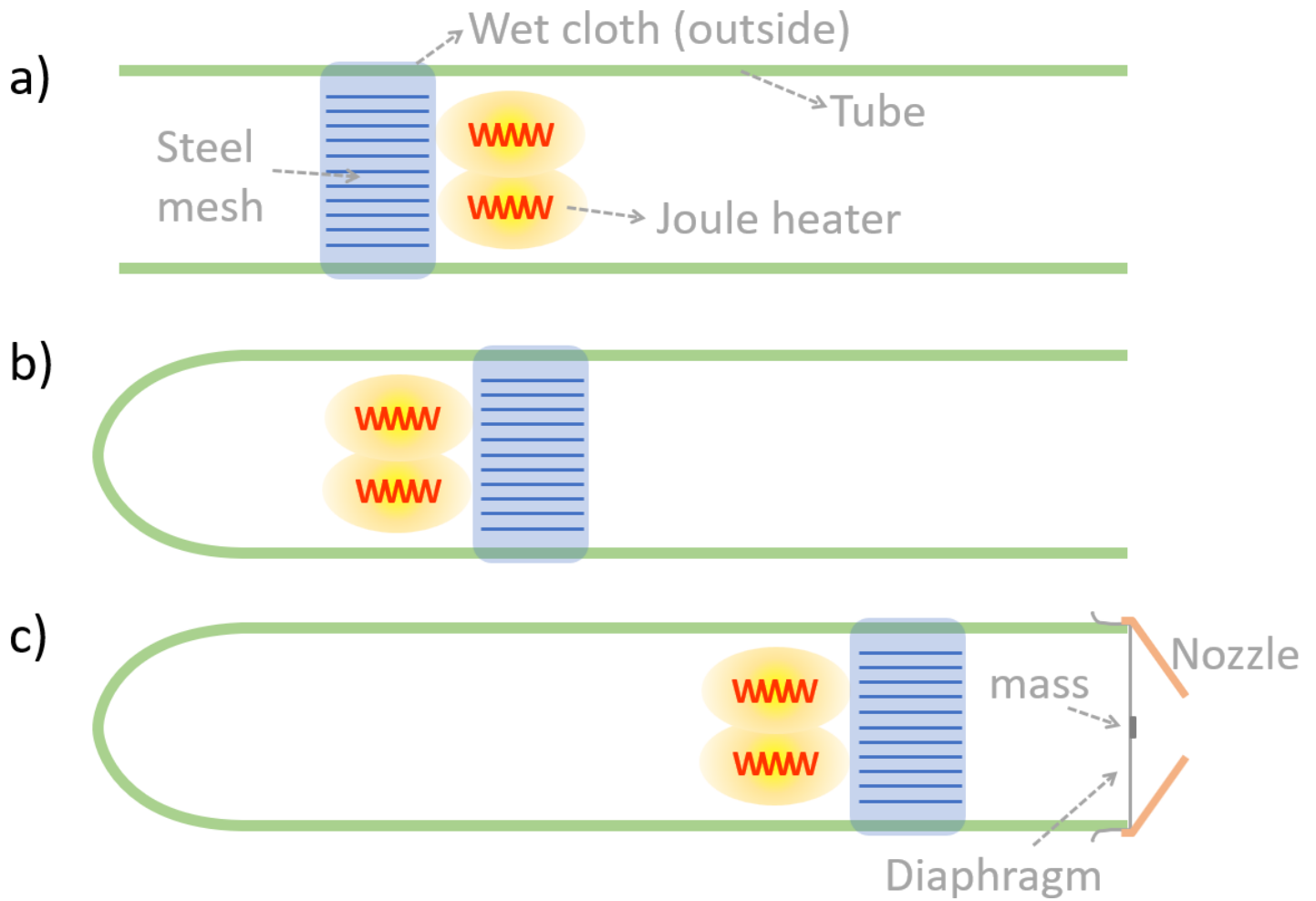


Figure 9

The three different tested configurations of thermoacoustic drivers for synthetic jets. (a) A horizontal Rijke tube. (b) A Sondhauss tube. (c) A vibrating diaphragm thermoacoustic engine.

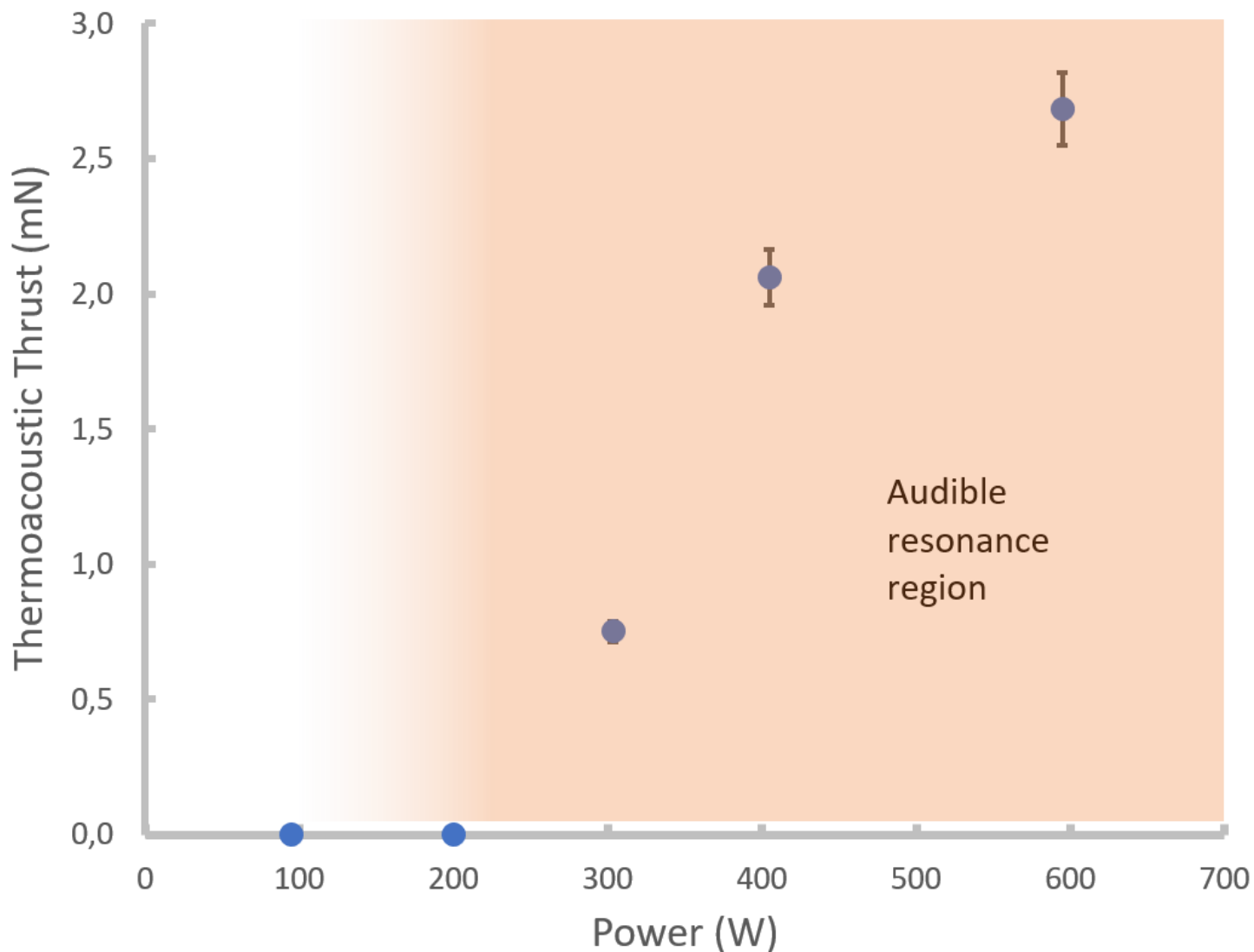


Figure 10

Thermoacoustic thrust as a function of Joule heating power with a Sondhaus configuration (Fig 9b). Thermoacoustic resonance and measurable thrust happened only for powers above 200W.

Supplementary Files

This is a list of supplementary files associated with this preprint. Click to download.

- [Fig3aGIF.gif](#)
- [Fig3bGIF.gif](#)
- [Fig3cGIF.gif](#)
- [Fig3dGIF.gif](#)